Chemical Science

ROYAL SOCIETY OF CHEMISTRY

EDGE ARTICLE

View Article Online
View Journal | View Issue



Cite this: *Chem. Sci.*, 2025, **16**, 9905

All publication charges for this article have been paid for by the Royal Society of Chemistry

# Boosting hydrogen evolution *via* flexoelectric catalysis in gradient F-doped hydroxyapatite nanowires†

Yucheng Zhang,[a] Jiawei Huang,[a] Lei Jiang,[b] Jun Qiang,[c] Zhouyang Zhang,[d] Zhanfeng Liu,[e] Yi Liu,[e] Tingfang Tian,*[a] Zhao Wang*[b] and Linfeng Fei*[a]

Received 26th January 2025
Accepted 26th April 2025

DOI: 10.1039/d5sc00710k

rsc.li/chemical-science

The emergence of flexoelectric effect, which refers to the linear electromechanical coupling between strain gradient and charge polarization in a wide range of materials, suggests a new catalytic mechanism to activate chemical bonds and reactions. Although pioneering studies have shown the remarkable potential for flexoelectric catalysis in a few scenarios, the lack of green, cheap, bio-compatible, and high-efficiency flexoelectric catalysts acts as a major barrier to its expanding applications. In this study, we report the effective design of a high-performance flexoelectric catalyst by simultaneous structural and compositional engineering on hydroxyapatite, a ubiquitous mineral and a well-known biomaterial. By synergizing atomic-scale and nanoscale strain gradients (which are respectively induced by surface lattice doping and geometry engineering) in F-doped hydroxyapatite nanowires (F-HAP NWs), the flexoelectric response together with the catalytic performance of the material are drastically improved, leading to a high hydrogen generation rate (322.7 μmol $g^{-1}$ $h^{-1}$) in pure water. The findings highlight the potential of F-HAP NWs in flexoelectric catalysis and offer new insights into mechanocatalytic and electrochemical processes in biological systems.

## Introduction

Flexoelectricity refers to the electromechanical coupling effect originating from the interaction between the gradient of a mechanical strain and the electric polarization of materials (*e.g.* insulating solids, liquid crystals, biological membranes).[1,2] Evidently, the applications of random external stress on materials usually introduce non-uniform strains as well as internal strain gradients,[3,4] which can break the inversion symmetry[5,6] and thereby generate polarization fields in samples.[7,8] Since flexoelectricity is not constrained by material symmetry, Curie temperature, or size (in contrast to the well-known piezoelectricity),[9] its widespread existence provides a new opportunity for harvesting and transforming mechanical energy from environmental vibrations such as waves and wind to drive electrochemical reactions (*i.e.*, flexoelectric catalysis).[10] Although the magnitude of the flexoelectric effect is generally small ($\sim 10^{-9}$ C $m^{-2}$ in terms of flexoelectric polarization) as compared to the piezoelectricity, it exists in all insulating materials while piezoelectricity is limited to non-centrosymmetric dielectrics.[11] Moreover, as a strain gradient is inversely proportional to the spatial scale of a system, the flexoelectric effect is size-dependent; therefore, flexoelectricity becomes increasingly conspicuous as the material size diminishes to the nanoscale.[12] In this context, recent studies have reported the emerging applications of flexoelectric catalysis in a few nanomaterials, primarily focusing on dye degradation,[13] $H_2O_2$ generation,[14] hydrogen evolution,[15] *etc.* For example, Cheng *et al.* have found that $Ag_2MoO_4$, as a flexoelectric catalyst, effectively degrades mixture dyes and other organic pollutants under ultrasonic irradiation.[16] Wu *et al.* have synthesized high-entropy oxide nanocomposites with $Ag(CuZn)(AlCr)_2O_4$ and CuO phases, where the interface strain gradients enhance the flexoelectric polarization and lead to an excellent hydrogen production rate under ultrasonic irradiation.[17] However, it is noticeable that those available flexoelectric catalysts are generally complex metal oxides, and always contain precious (Au, Ag, Pt, *etc.*) or heavy metal elements (Cd, Pb, Sn, *etc.*), resulting in intricate synthesis protocols, high costs, and potential environmental/health risks.[18–20] Thus, the search of high-performance

[a]*School of Physics and Materials Science, Jiangxi Provincial Key Laboratory of Photodetectors, Nanchang University, Nanchang, Jiangxi 330031, P. R. China. E-mail: feilinfeng@gmail.com; tftian@ncu.edu.cn*

[b]*Hubei Key Laboratory of Micro- & Nanoelectronic Materials and Devices, School of Microelectronics, Hubei University, Wuhan, Hubei 430062, P. R. China. E-mail: wangzhao@hubu.edu.cn*

[c]*School of Mechanical Engineering, Ningxia University, Yinchuan, Ningxia 750021, P. R. China*

[d]*School of Materials and New Energy, Ningxia University, Yinchuan, Ningxia 750021, P. R. China*

[e]*National Synchrotron Radiation Laboratory, University of Science and Technology of China, Hefei, Anhui 230029, P. R. China*

† Electronic supplementary information (ESI) available. See DOI: https://doi.org/10.1039/d5sc00710k

flexoelectric catalysts that are both eco-friendly and cost-effective, is an urgent task.

As a common natural mineral and also the major component of bones, the centrosymmetric hydroxyapatite ($Ca_{10}(PO_4)_6(OH)_2$, abbreviated as HAP) has also been proven to exhibit flexoelectricity,[21,22] implying its potential to serve as a green, cheap, and bio-compatible flexoelectric catalyst.[23] However, the observed flexoelectric effect is normally subtle, which may lead to poor flexoelectric catalytic performance. To boost the catalytic performance of HAP, it is of first priority to improve its flexoelectric response (*i.e.*, flexoelectric polarization charges).[24–26] In this event, it is thereby essential to increase the deformation limit under external forces of its nanomaterials; consequently, according to previous reports, it is anticipated that controlling the geometry of HAP nanomaterials in the form of 1D (one-dimensional) nanowires (NWs) or 2D (two-dimensional) nanoflakes, which both allow large degrees of deformation without breaking their structural integrities at the nanoscale, is a convenient and well developed strategy.[27–29] Previously, we have demonstrated that methylammonium lead iodide ($MAPbI_3$) NWs are more easily to be bent than its nanoparticles counterpart, which therefore leads to a higher flexoelectric response.[30] Similarly, it is also rather beneficial if additional local strain could be introduced into HAP nanomaterials.[31,32] For instance, Wu *et al.* have systematically characterized the nanoscale flexoelectricity and demonstrated the ability to achieve tunable and large strain gradients at the atomic-scale grain boundaries.[33] In light of this case, surface lattice doping (or in other words, gradient doping) should be effective in creating atomic-scale strain gradients for those 1D & 2D nanomaterials.[34]

Inspired by the above discussions, we report herein the gradient F-doped HAP (F-HAP) NWs as a new type of high-performance flexoelectric catalyst for hydrogen evolution reaction. High aspect-ratio F-HAP NWs were synthesized for the catalytic application, which are capable of generating significant nanoscale strain gradients under mechanical stimulation. Besides, the isoelectronic nature of fluoride ions ($F^-$) and hydroxide groups ($OH^-$) allows for partial substitutions of $OH^-$ by $F^-$ within the lattices of HAP, and the size mismatch of $F^-$ and $OH^-$ introduces local strain in HAP; moreover, the favorable strain gradient can be also introduced in HAP NWs upon a controlled surface doping strategy.[35,36] Therefore, the coupling of the nanoscale and atomic-scale strain gradients induces a significantly enhanced flexoelectric response of F-HAP NWs, resulting in a high hydrogen generation rate (322.7 μmol $g^{-1}$ $h^{-1}$ in pure water, which is comparable with state-of-the-art mechanocatalysts) in flexoelectric catalysis. This study offers novel design concepts for flexoelectric catalysts in chemical reactions and has the potential to address a gap in the field of mechanocatalysis.

## Results and discussion

To systematically investigate the effect of nanoscale and atomic-scale strain gradients on the performance of flexoelectric catalysis, HAP NWs with different F-doping levels and different aspect ratios were parallelly synthesized by a modified hydrothermal method (see Experimental section and Table S1† for details).[37] For short, F-HAP NWs with different $F^-$ concentrations were named as HAP, F(1)-HAP, F(3)-HAP, F(5)-HAP, and F(7)-HAP, where the $F^-$ concentration was set as 0%, 1%, 3%, 5% and 7%, respectively; and F(5)-HAP NWs (which has the best catalytic performance among the above five samples; refer to the following discussion) with increasing aspect ratios were named as S-HAP, M-HAP, and L-HAP, where S, M, and L stand for Short, Middle, and Long, respectively (see Fig. S1† for the statistical analysis of their diameters and lengths).

A multiscale characterization was initially conducted across the F-HAP samples to examine the structural information. Fig. 1a presents the typical scanning electron microscopy (SEM) image of a crowd of F-HAP NWs, which reveals their characteristic 1D microstructures and smooth surfaces, with an average diameter of 50 nm and lengths up to 1000 nm. It should be noted that a few NWs were markedly bent under SEM observations, showing their highly flexible characteristics. High-resolution transmission electron microscopy (HRTEM) image (Fig. 1b) exhibits the orthogonal lattice fringes with interplanar spacings of 0.35 and 0.47 nm, corresponding to the (002) and (110) planes of hexagonal HAP, respectively. A slight decrease in the F-HAP crystal plane spacing is observed in comparison to the undoped HAP nanowires (Fig. S2 and S3†). Fast Fourier transform (FFT) pattern from an isolated NW (inset in Fig. 1b) confirms its single-crystalline nature, with the pattern well assigned to a hexagonal structure as reported in previous synthesis. High-angle annular dark-field scanning transmission electron microscopy (HAADF-STEM) image of a HAP NW is presented in Fig. 1c, clearly showing the homogeneous lattices from the surface to the center of the 1D structure. HAADF-STEM image in Fig. 1d further demonstrates the smooth surface of a representative NW. Fig. 1e–h presents the energy dispersive spectroscopy (EDS) elemental mappings for Ca, O, and P within the selected NW. The synchronous distributions of these constituent elements imply a uniform chemical composition. However, the distribution pattern of fluorine (F) differs from those of P, Ca, and O. It can be identified that the concentration of F gradually decreases from the surface to the center of the NWs, which could be ascribed to the diffusion gradient of F doping (see Fig. S4† for a dedicated EDS line scan result). In order to directly visualize the strain distributions across the NWs, geometric phase analysis (GPA) based on the HAADF-STEM images of F-HAP NWs was performed in the selected regions in Fig. 1i and j (the interior region and the surface region of NWs, respectively). As shown in Fig. 1k and l, GPA mappings reveal that the $E_{yy}$ strain component at the surface region is significantly higher than that from the interior region, suggesting lattice distortions at the surface of the NW (mainly due to gradient F doping).

The crystal structure of the F-HAP samples was subjected to further investigation *via* X-ray diffraction (XRD). As shown in Fig. 1m, the diffraction patterns from all F-HAP NWs correspond to the hexagonal phase of HAP. The diffraction peaks observed at 25.87°, 31.77°, 32.20°, and 32.90° are assigned to the crystal planes of HAP, namely (002), (211), (112), and (300), respectively. As the concentration of F elements increases, the

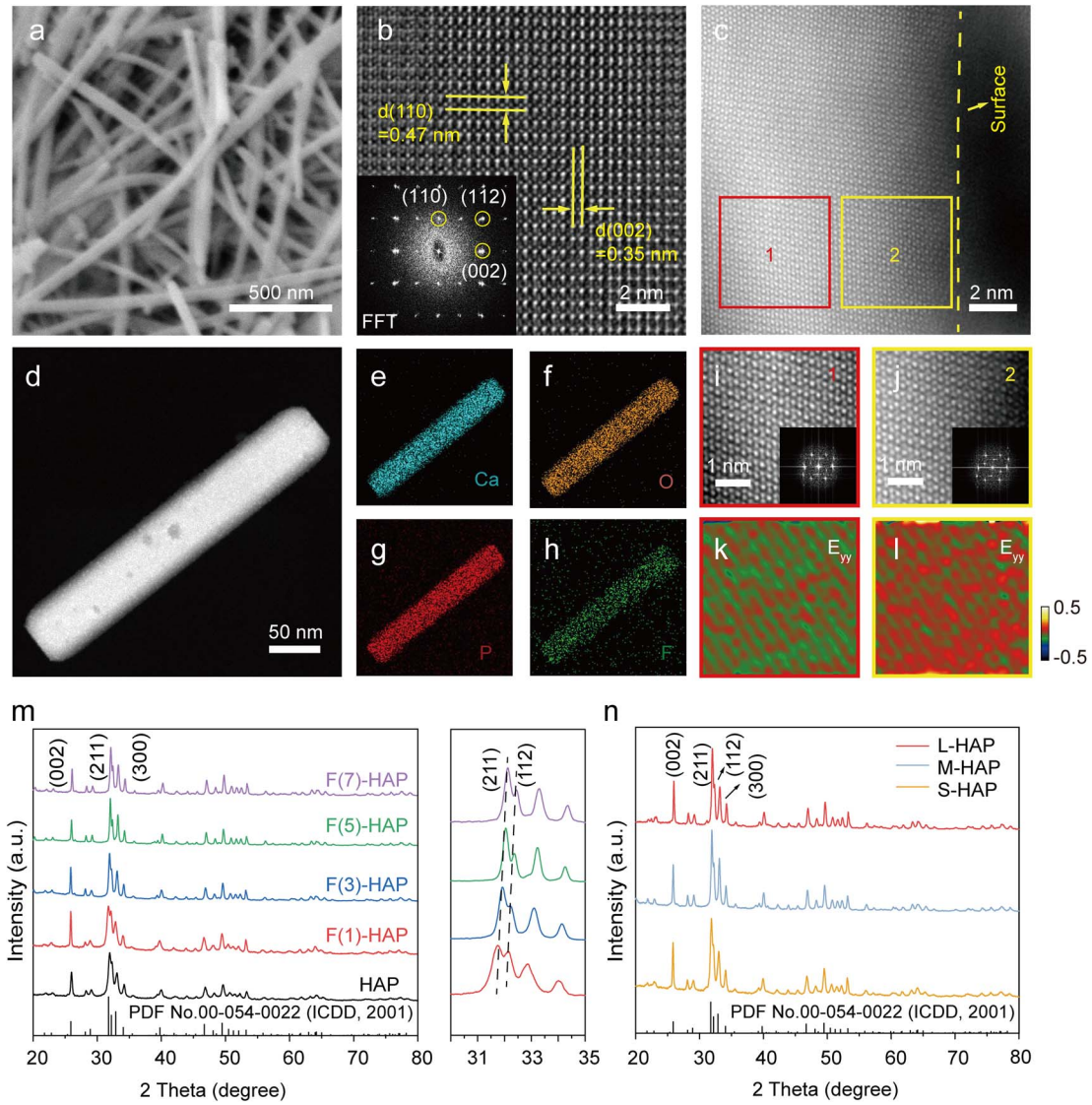


Fig. 1 Structural characterizations for F-HAP samples. (a) SEM image, (b) lattice-resolved HRTEM image (inset: FFT pattern), (c and d) HAADF-STEM images, and (e–h) EDS elemental mappings for Ca, O, P and F of (d) for F(5)-HAP NWs. (i and j) Enlarged views for regions 1 and 2 in (c). (k and l) GPA analysis for regions 1 and 2. (m) XRD patterns for HAP, F(1)-HAP, F(3)-HAP, F(5)-HAP, and F(7)-HAP. (n) XRD patterns for S-HAP, M-HAP, and L-HAP.

(211) and (112) crystal planes are observed to shift to higher angles in the right panel of Fig. 1m, indicating the successful incorporation of F atoms into HAP NWs.[38] The above changes should be caused by the gradient doping of smaller $F^-$ (133 pm) in the original HAP lattice framework containing $OH^-$ (137 pm), resulting in partial lattice distortions. Besides, TEM observations (Fig. S5†) also reveal distinct dislocations at the surface of F-HAP NWs due to the gradient doping of F, confirming that the doping successfully induced lattice distortions and introduced atomic-scale strain gradients (see further discussions below). According to these results, the surface of F-HAP NWs is thereby strained due to the controlled introduction of F doping. In addition, XRD patterns of F(5)-HAP NWs with different aspect ratios maintain the same as the standard card (Fig. 1n).

Subsequently, to understand the surface chemistry of F-doped HAP NWs, X-ray photoelectron spectroscopy (XPS) was performed, showcasing the existence of expected elements in the samples (Fig. 2a). Moreover, as shown in Fig. 2b, the fine scan of F 1s in F(5)-HAP shows a peak at 684 eV, indicating the presence of F.[39] The lattice oxygen ratio in F(5)-HAP decreases, and the chemical states of P 2p, and Ca 2p in F(5)-HAP are similar to those in HAP (Fig. S6†). Fourier transform infrared spectroscopy (FTIR) was used to analyse the chemical structures of the F-HAP samples. The results of FTIR analysis (Fig. 2c) indicate the emergence of a new absorption peak at 736 $cm^{-1}$ in F-doped HAP NWs (this peak can be attributed to the F···OH stretching vibration[40]) as the concentration of F doping increases. The bending vibration peaks of P–O bond in $PO_4^{3-}$ appear at 563 $cm^{-1}$ and 604 $cm^{-1}$, and the tensile vibration peaks are located at 962 $cm^{-1}$, 1031 $cm^{-1}$, and 1099 $cm^{-1}$.[41] The results showed that F doping did not change the characteristic

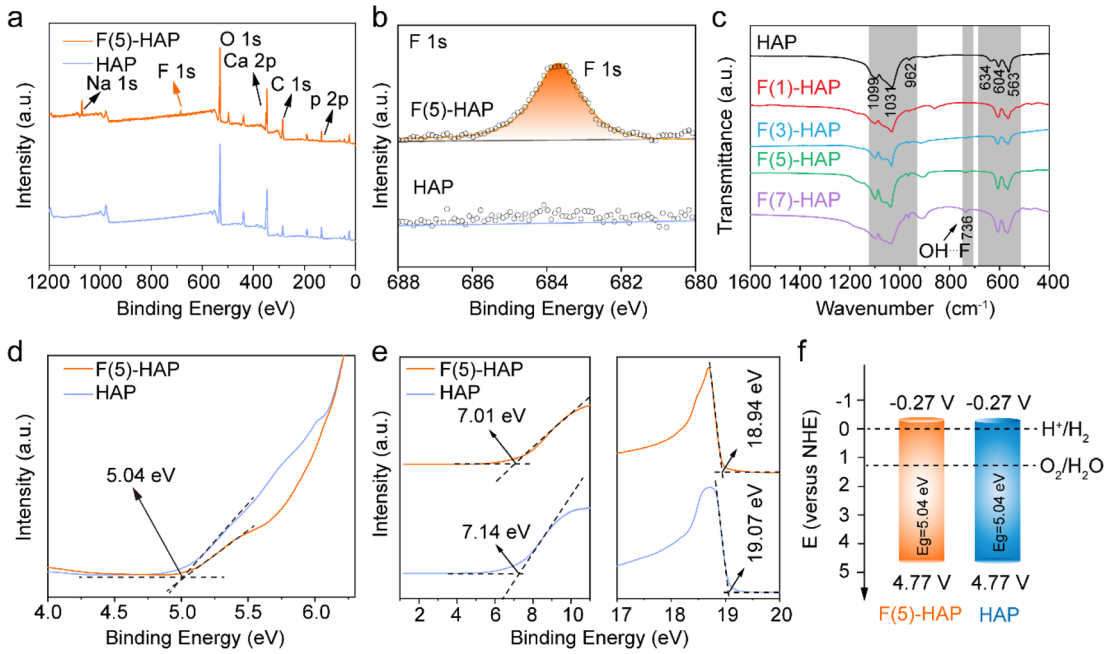


Fig. 2 Optical characterizations for F-HAP samples. (a) XPS survey spectra and (b) F 1s high-resolution XPS spectra of F(5)-HAP and HAP. (c) FTIR profiles of F-HAP samples. (d) Tauc plots and (e) UPS spectra of F(5)-HAP and HAP samples. (f) Band structures of F(5)-HAP and HAP for hydrogen generation reaction.

functional groups of $PO_4^{3-}$ in HAP, but only introduced the F⋯OH bonds.[42]

The optoelectronic properties and energy band structure of the samples were also characterized. The optical absorbances of F-HAP NWs were investigated by UV-visible absorption spectroscopy (Fig. S7†). The absorption edges of F-HAP do not exhibit significant alterations in comparison to HAP.[43] Fig. 2d presents the Tauc plot for the optical bandgap of F-HAP NWs and HAP (5.04 eV). To determine the effect of F doping on the energy bands of HAP, ultraviolet photo-electron spectroscopy (UPS) tests were performed. Fig. 2e shows the positions of the valence band (VB) and the work function ($W_f$) for HAP and F(5)-HAP, respectively. VB of HAP is approximately 7.14 eV, and $W_f$ is 19.07 eV. In comparison, the VB of F(5)-HAP is 7.01 eV, and $W_f$ is 18.94 eV (Fig. S8† compares the optical bandgaps of F(5)-HAP and HAP). The conduction band minimum (CBM) and valence band maximum (VBM) of F(5)-HAP correspond to −0.27 V and 4.77 V relative to the normal hydrogen electrode (NHE), respectively (Fig. 2f). As shown in the band structure map, F doping has minimally affected the energy levels. It is noteworthy that this energy level alignment of F-HAP is consistent with the thermodynamic requirements for water splitting, dictated by the electrode potential of $H^+/H_2$ (0.00 V *versus* NHE) and $O_2/H_2O$ (+1.23 V *versus* NHE).

Piezoelectric force microscopy (PFM) mode of a scanning probe microscope (SPM) was employed to assess the electromechanical coupling behaviour of F-HAP NWs; both L-HAP and S-HAP were involved in this test to compare their PFM response.[44] The applied voltage through the PFM tip induced a mechanical response in F-HAP NWs, confirming electromechanical coupling in both NWs. It can be observed that the biasing of L-HAP and S-HAP-NWs yielded typical amplitude-voltage butterfly loops (with their maximum amplitudes at 136.19 and 70.91 pm, respectively; see Fig. 3a and c) and distinct 180° phase-reversal hysteresis loops as the flexoelectric response (Fig. 3b and d). Apparently, the displacement of S-HAP NWs is smaller than that of L-HAP NWs, which demonstrates that L-HAP NWs exhibit a larger flexoelectric response; the amplitude curves indicate that the $d_{33}$ piezoelectric coefficient for L-HAP NWs (24.47 pm $V^{-1}$) is much greater than that of S-HAP NWs (11.33 pm $V^{-1}$). These observations suggest an exceptional electromechanical coupling in these F-HAP NWs, which agrees well with the existing reports indicating that F-HAP exhibits a superior flexoelectric response relative to HAP.[38] Fundamentally, the introduction of a strain gradient through gradient $F^-$ doping enhances the flexoelectric response in HAP NWs. Likewise, our experiments indicate that the aspect ratio of F-HAP NWs also influences the flexoelectric response. L-HAP, which experiences a larger strain gradient during deformation, shows a more significant flexoelectric response compared to S-HAP. The combined effect of deformation-induced strain and F doping significantly enhances the overall flexoelectric response in L-HAP NWs.

Moreover, finite element method (FEM) was employed to model the strain gradient of single NWs subjected to a bending stress. To simulate NWs of varying lengths under the same stress condition, three individual models were created with the lengths of 300 (Fig. 3e), 600 (Fig. S9†), and 1000 nm, and all with a fixed diameter of 50 nm. Fig. 3f illustrates the stress distributions ($\varepsilon_{11}$) within NWs under bending moments applied at both ends. Clearly, one side (red area) experiences a tensile stress, while the opposite side (blue area) experiences

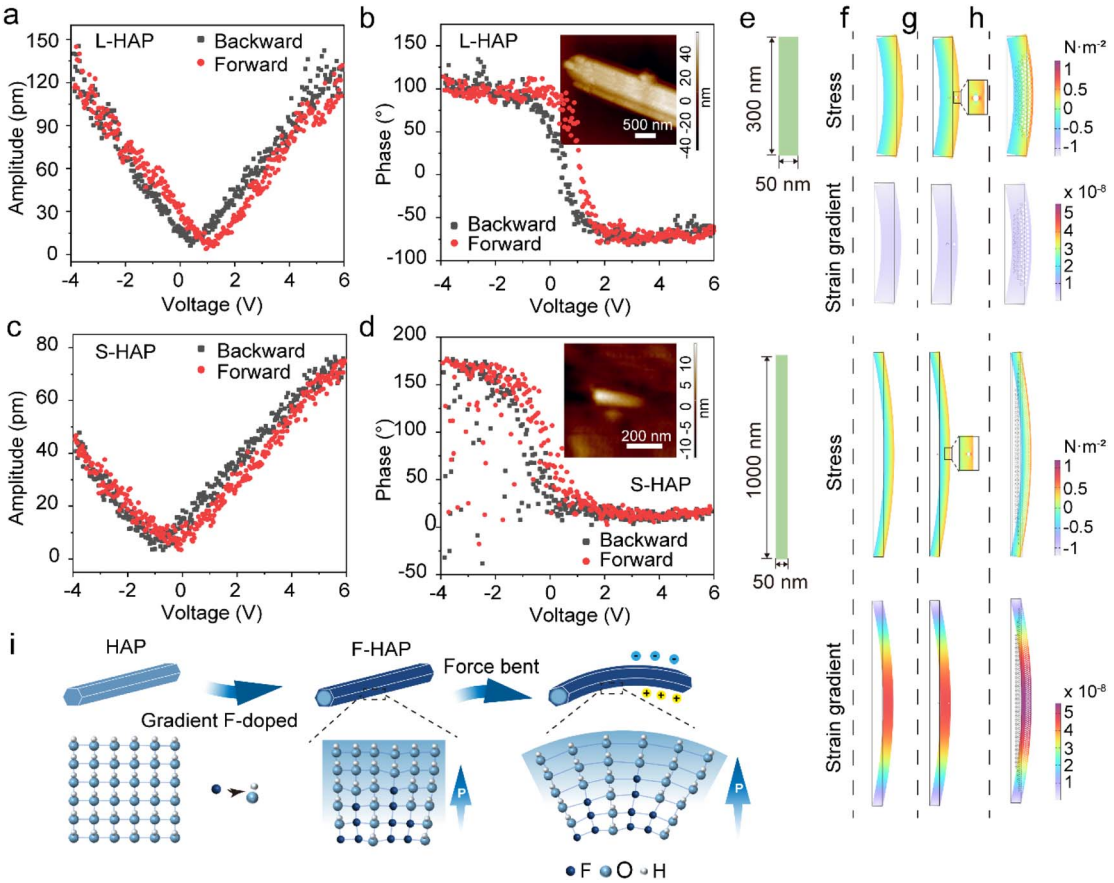


Fig. 3 Bending behaviours of F-HAP NWs. (a) PFM response and (b) phase curve for an L-HAP NW (inset of (b): the corresponding PFM image). (c) PFM response and (d) phase curve for an S-HAP NW (inset of (d): the corresponding PFM image). (e) FEM models for S-HAP and L-HAP NWs. (f) FEM results for bending induced stress and strain gradient distributions within F-HAP NWs. (g) FEM results for bending induced stress and strain gradient upon doped with one atom within F-HAP NWs. (h) FEM results for bending induced stress and strain gradient upon surface doping within F-HAP NWs. (i) Schematic illustration for the coupling of F-gradient doping and strain gradient in a bending HAP NW.

a compressive stress (the green area represents the neutral plane, where $\varepsilon = 0$). Consequently, in this event, strain increases gradually from the center to the surface along the radial direction and decreases from the center toward the ends along the axial direction. Under identical stress conditions, the long NW exhibits greater deformation compared to the short one, resulting in a more pronounced strain gradient. The strain gradients are relatively low at both ends of NWs but show a significant increase in the central regions. This finding demonstrates that a high aspect ratio of NWs facilitates the formation of strain gradients, thereby enhancing the mechanoelectrical coupling. The simulation shown in Fig. 3g examines the effect of a single doping atom within the NWs. While the overall stress distribution remains largely unchanged upon bending, a notable concentration of stress is observed at the doped sites, as shown in the enlarged frames. Finally, the simulation presented in Fig. 3h illustrates the stress distributions and strain gradients of NWs during bending upon surface doping (*i.e.*, gradient doping) of foreign atoms. As gradient doping progresses, the stresses on both the tensile and compressive sides of NWs increase, accompanied by significant rises in the strain gradients.

Based on the above results and analysis, Fig. 3i proposes the potential flexoelectric mechanism in the F-HAP NWs. Since the radius of $F^-$ is slightly smaller than that of $OH^-$, the surface doping of $F^-$ in HAP NWs introduces lattice compression and generates atomic-scale strain gradients in F-HAP NWs, which could significantly enhance the flexoelectric effects. Meanwhile, external mechanical stimulations (such as ultrasound) would induce substantial bending for these flexible NWs, resulting in nanoscale strain gradients caused by the deformation. The coupling of strain gradients induced by lattice distortions and NWs deformation enhances the overall flexoelectric effect; the internal polarization field thereby promotes the separation of electrons and holes in opposite directions.[15] Besides, it should also be mentioned that the internal electric field can cause the energy bands to tilt.[45] Consequently, protons ($H^+$) in the water rapidly bind to the accumulated charge, resulting in the production of $H_2$.

Based on the preceding analysis, we expect that F-HAP NWs would exhibit a remarkable flexoelectric catalytic performance for hydrogen evolution. Therefore, we investigated the flexoelectric catalytic performance of F-HAP NWs upon ultrasonic stimulation in a dark environment. F-HAP NWs were added into a self-made quartz reactor, filled with deionized water, sealed,

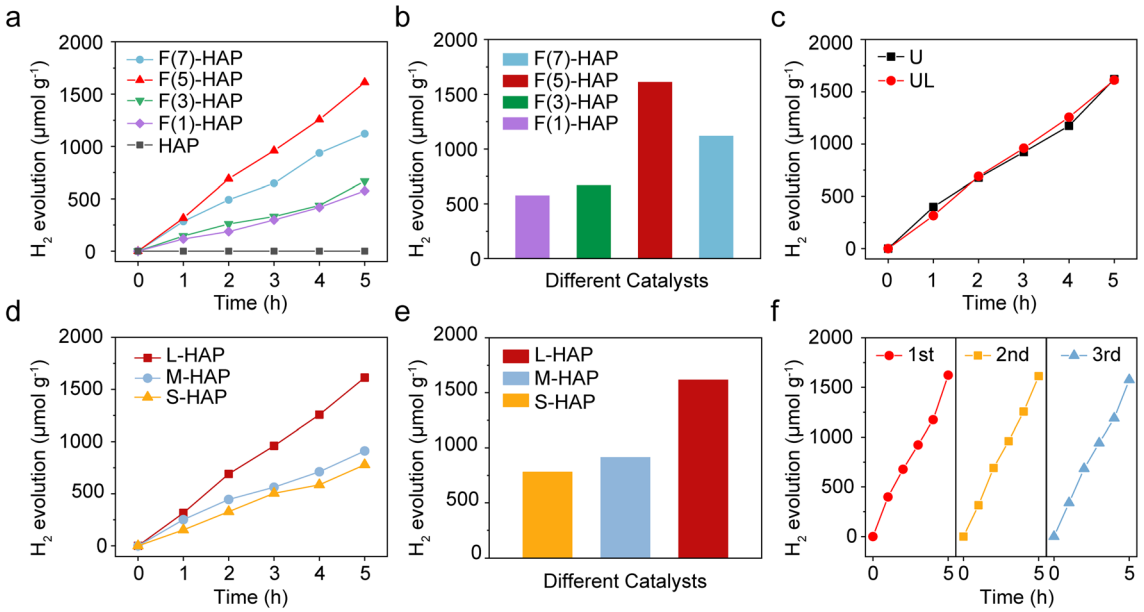


Fig. 4 Hydrogen production performances of F-HAP NWs *via* flexoelectric catalysis. (a) Time-dependent hydrogen evolution profiles for HAP and F-HAP NWs. (b) Comparative amounts of hydrogen generated from F-HAP NWs after 5 h. (c) Time-dependent hydrogen evolution profiles for F(5)-HAP NWs under ultrasonic (black) and ultrasonic/light (red). (d) Time-dependent hydrogen evolution profiles for S-HAP, M-HAP and L-HAP NWs. (e) Comparative amounts of hydrogen produced by HAP NWs with different aspect ratios (S, M and L) after 5 h. (f) Cycling performance of hydrogen generation for F(5)-HAP NWs.

and subjected to ultrasound-induced mechanical actions. Gas chromatography (GC) was employed to monitor the $H_2$ produced by the reaction system. The experiment has demonstrated that F-HAP has the capability to produce $H_2$ under mechanical stimulation. Fig. 4a shows the catalytic performance of F-HAP NWs with different levels of F doping, all exhibiting a strong and linear hydrogen production over time, and F(5)-HAP achieved the highest $H_2$ yield of 322.7 μmol $g^{-1}$ $h^{-1}$ (the original GC data can be referred in Fig. S10†). Fig. 4b summarizes the $H_2$ yields over 5 h for different F doping levels, which are 575.7, 668.6, 1613.3, and 1121.5 μmol $g^{-1}$ from lowest to highest doping levels. It is evident that F gradient doping significantly enhances the interactions between F-HAP NWs and mechanical signals (it should be mentioned that the surface $F^-$ doping strategy may induce localized symmetry breaking in HAP NWs, thereby introducing possible piezoelectric effect in the catalysis), yet an appropriate level of F doping is crucial for achieving the highest flexoelectric response as well as catalytic efficiency. To verify the absence of light effect, an external light source (xenon lamp) was used to continuously irradiate the reactor under the same experimental conditions. The results showed that the catalytic activity of F-HAP did not depend on light (Fig. 4c), but solely on mechanical interaction.

As mentioned earlier, catalysts based on flexoelectric effect offer a significant advantage, particularly at the nanoscale, where the flexoelectric effect becomes more pronounced as the dimensions decrease. F(5)-HAP NWs with different aspect ratios, namely L-HAP, M-HAP, and S-HAP, were further tested for their catalytic properties. As shown in Fig. 4d, L-HAP NWs had higher $H_2$ production efficiency (the original GC data can be referred in Fig. S11†). Quantitatively, there was a significant enhancement of hydrogen production from 778.3 to 1613.3 μmol $g^{-1}$ for F-HAP NWs with the increase in aspect ratios (Fig. 4e). Consistent with previous FEM findings, L-HAP NWs can produce greater deformation under mechanical stimulation, which in turn causes a larger strain gradient and thus a better catalytic activity. The cyclic stability of F-HAP NWs as catalysts for hydrogen production in flexoelectric catalysis was also assessed; as shown in Fig. 4f. The hydrogen production rate remained constant throughout three catalytic cycles (a total duration of 15 h), suggesting that the F-HAP NWs have good reproducibility and durability in this catalytic reaction. To the best of our knowledge, as a biomaterial, the catalytic ability of F-HAP NWs is already comparable to those of some familiar catalytic materials (Table S2†). Besides, we comprehensively analysed the microstructural evolution of F-HAP NWs during the reaction. Compared with the XRD pattern of the pre-reaction material (Fig. S12†), the peak of F-HAP remained almost unchanged after the reaction, indicating that it was stable in the catalytic system. In addition, the NWs after 3 cycles (15 h) were isolated from the reaction system and further observed under SEM (Fig. S13†). During the prolonged reaction, the NWs were fractured and fragmented to a certain extent due to the destructive effect of ultrasound, but their 1D structures remained unchanged.

## Conclusions

In summary, we have synthesized HAP NWs with controllable surface F doping and investigated their application for flexoelectrically catalysing hydrogen generation in pure water. Our results show that the nanoscale strain gradient can be enhanced

by increasing the aspect ratio of NWs while an additional atomic-scale strain gradient could be introduced by the F-doping gradient at the surface regions of NWs. The synergistic effect of the nanoscale and atomic-scale strain gradients by respectively optimizing the aspect ratio and F doping level leads to a significant flexoelectric response for HAP NWs. As a result, a high hydrogen production rate of 322.7 μmol $g^{-1}$ $h^{-1}$ is achieved in pure water *via* flexoelectric catalysis in darkness. Our work demonstrates the potential of HAP NWs for hydrogen production by harvesting mechanical energy from environment, offering great promise for flexoelectric research on centrosymmetric and bio-compatible materials.

## Data availability

All data needed to evaluate the conclusions are present in the article and/or the ESI.†

## Author contributions

L. F. conceived and supervised the project. L. F. and Y. Z. designed experiments. J. H. conducted TEM analysis. Z. W. and L. J. conducted PFM tests. J. Q. and Z. Z. performed FEM calculations. Y. L. and Z. L. conducted UPS measurements. Y. Z., T. T. and L. F. wrote the manuscript with the help and input from all authors. All authors have given approval to the final version of the manuscript.

## Conflicts of interest

There are no conflicts to declare.

## Acknowledgements

This work was supported by the National Natural Science Foundation of China (22375081 and U21A20500) and the Jiangxi Provincial Natural Science Foundation (20212ACB204016). L. F. also acknowledges the support from Nanchang University.

## References

1 L. Shu, R. Liang, Z. Rao, L. Fei, S. Ke and Y. Wang, Flexoelectric materials and their related applications: A focused review, *J. Adv. Ceram.*, 2019, **8**, 153.
2 L. Wang, S. Liu, X. Feng, C. Zhang, L. Zhu, J. Zhai, Y. Qin and Z. L. Wang, Flexoelectronics of centrosymmetric semiconductors, *Nat. Nanotechnol.*, 2020, **15**, 661.
3 T. D. Nguyen, S. Mao, Y. W. Yeh, P. K. Purohit and M. C. McAlpine, Nanoscale flexoelectricity, *Adv. Mater.*, 2013, **25**, 946.
4 L. E. Cross, Flexoelectric effects: Charge separation in insulating solids subjected to elastic strain gradients, *J. Mater. Sci.*, 2006, **41**, 53.
5 X. Jiang, W. Huang and S. Zhang, Flexoelectric nano-generator: Materials, structures and devices, *Nano Energy*, 2013, **2**, 1079.
6 L. Shu, Z. Yong, X. Jiang, Z. Xie and W. Huang, Flexoelectricity in low densification materials and its implication, *J. Alloys Compd.*, 2017, **695**, 1555.
7 P. V. Yudin and A. K. Tagantsev, Fundamentals of flexoelectricity in solids, *Nanotechnology*, 2013, **24**, 432001.
8 A. Biancoli, C. M. Fancher, J. L. Jones and D. Damjanovic, Breaking of macroscopic centric symmetry in paraelectric phases of ferroelectric materials and implications for flexoelectricity, *Nat. Mater.*, 2015, **14**, 224.
9 R. A. Surmenev and M. A. Surmeneva, The influence of the flexoelectric effect on materials properties with the emphasis on photovoltaic and related applications: A review, *Mater. Today*, 2023, **67**, 256.
10 Z. Liu, X. Wen, Y. Wang, Y. Jia, F. Wang, G. Yuan and Y. Wang, Robust flexo-catalysis in centrosymmetric nanoparticles, *Adv. Mater. Technol.*, 2022, **7**, 2101484.
11 B. Wang, Y. Gu, S. Zhang and L. Q. Chen, Flexoelectricity in solids: Progress, challenges, and perspectives, *Prog. Mater. Sci.*, 2019, **106**, 100570.
12 Z. Wang, C. Li, H. Xie, Z. Zhang, W. Huang, S. Ke and L. Shu, Effect of grain size on flexoelectricity, *Phys. Rev. Appl.*, 2022, **18**, 064017.
13 K. Liu, T. Wu, L. Xu, Z. Zhang, Z. Liu, L. Wang and Z. L. Wang, Flexo-photocatalysis in centrosymmetric semiconductors, *Nano Res.*, 2024, **17**, 1173.
14 H. Tan, W. Si, W. Peng, X. Chen, X. Liu, Y. You, L. Wang, F. Hou and J. Liang, Flexo-/piezoelectric polarization boosting exciton dissociation in curved two-dimensional carbon nitride photocatalyst, *Nano Lett.*, 2023, **23**, 10571.
15 Y. Du, S. Zhang and Z. Cheng, Flexocatalysis of nanoscale titanium dioxide, *Nano Energy*, 2024, **127**, 109731.
16 T. Cheng, H. Gao, R. Li, S. Wang, Z. Yi and H. Yang, Flexoelectricity-induced enhancement in carrier separation and photocatalytic activity of a photocatalyst, *Appl. Surf. Sci.*, 2021, **566**, 150669.
17 P. Y. Wu, K. T. Le, H. Y. Lin, Y. C. Chen, P. H. Wu and J. M. Wu, Flexoelectric catalysts based on hierarchical wrinkling surface of centrosymmetric high-entropy oxide, *ACS Nano*, 2023, **17**, 17417.
18 P. W. Shao, M. C. Lin, Q. Zhuang, J. Huang, S. Liu, H. W. Chen, H. L. Liu, Y. J. Lu, Y. J. Hsu, J. M. Wu, Y. C. Chen and Y. H. Chu, Flexo-phototronic effect in centro-symmetric $BiVO_4$ epitaxial films, *Appl. Catal., B*, 2022, **312**, 121367.
19 Y. C. Chen, P. H. Chen, Y. S. Liao, J. P. Chou and J. M. Wu, Defect engineering centrosymmetric 2D material flexocatalysts, *Small*, 2024, **20**, 2401116.
20 Z. Chen, H. Zhou, F. Kong and M. Wang, Piezocatalytic oxidation of 5-hydroxymethylfurfural to 5-formyl-2-furancarboxylic acid over Pt decorated hydroxyapatite, *Appl. Catal., B*, 2022, **309**, 121281.
21 F. Vasquez-Sancho, A. Abdollahi, D. Damjanovic and G. Catalan, Flexoelectricity in bones, *Adv. Mater.*, 2018, **30**, 1705316.
22 Y. Zhou, H. Wang, X. Liu, S. Qiao, D. Shao, J. Zhou, L. Zhang and W. Wang, Direct piezocatalytic conversion of methane

into alcohols over hydroxyapatite, *Nano Energy*, 2021, **79**, 105449.
23 S. Li, Y. Li, W. Shen, Y. Bai and L. Kong, Hydroxyapatite-based catalysis in environmental decontamination, *J. Cleaner Prod.*, 2022, **380**, 134961.
24 Y. Xia, W. Qian and Y. Yang, Advancements and prospects of flexoelectricity, *ACS Appl. Mater. Interfaces*, 2024, **16**, 9597.
25 P. Zubko, G. Catalan and A. K. Tagantsev, Flexoelectric effect in solids, *Annu. Rev. Mater. Res.*, 2013, **43**, 387.
26 S. Mao and P. K. Purohit, Defects in flexoelectric solids, *J. Mech. Phys. Solids*, 2015, **84**, 95.
27 T. Wu, K. Liu, S. Liu, X. Feng, X. Wang, L. Wang, Y. Qin and Z. L. Wang, Highly efficient flexocatalysis of two-dimensional semiconductors, *Adv. Mater.*, 2023, **35**, 2208121.
28 L. Sai, Y. Xiao, F. Yan, T. Ying, Z. Wu, H. Xu, Y. Jia and F. Wang, Integration of hydrogen evolution and dye removal in flexocatalysis by centrosymmetric semiconductor nanorods, *Int. J. Hydrogen Energy*, 2024, **69**, 944.
29 B. He, B. Javvaji and X. Zhuang, Size dependent flexoelectric and mechanical properties of barium titanate nanobelt: A molecular dynamics study, *Physica B*, 2018, **545**, 527.
30 Y. Zhang, J. Huang, M. Zhu, Z. Zhang, K. Nie, Z. Wang, X. Liao, L. Shu, T. Tian, Z. Wang, Y. Lu and L. Fei, Significant hydrogen generation *via* photo-mechanical coupling in flexible methylammonium lead iodide nanowires, *Chem. Sci.*, 2024, **15**, 1782.
31 S. Das, B. Wang, T. R. Paudel, S. M. Park, E. Y. Tsymbal, L. Q. Chen, D. Lee and T. W. Noh, Enhanced flexoelectricity at reduced dimensions revealed by mechanically tunable quantum tunnelling, *Nat. Commun.*, 2019, **10**, 537.
32 L. Zhang, Z. Wang, S. Shu, Y. Hu, C. Li, S. Ke, F. Li and L. Shu, Origin of defects induced large flexoelectricity in ferroelectric ceramics, *Phys. Rev. Mater.*, 2022, **6**, 094416.
33 M. Wu, X. Zhang, X. Li, K. Qu, Y. Sun, B. Han, R. Zhu, X. Gao, J. Zhang, K. Liu, X. Bai, X. Z. Li and P. Gao, Engineering of atomic-scale flexoelectricity at grain boundaries, *Nat. Commun.*, 2022, **13**, 216.
34 J. Narvaez, F. Vasquez-Sancho and G. Catalan, Enhanced flexoelectric-like response in oxide semiconductors, *Nature*, 2016, **538**, 219.
35 J. Read, Fluorine in the human skeleton, *Nature*, 1953, **172**, 1156.
36 L. M. Rodríguez-Lorenzo, J. N. Hart and K. A. Gross, Influence of fluorine in the synthesis of apatites. Synthesis of solid solutions of hydroxy-fluorapatite, *Biomaterials*, 2003, **24**, 3777.
37 B. Ma, S. Zhang, F. Liu, J. Duan, S. Wang, J. Han, Y. Sang, X. Yu, D. Li, W. Tang, S. Ge and H. Liu, One-dimensional hydroxyapatite nanostructures with tunable length for efficient stem cell differentiation regulation, *ACS Appl. Mater. Interfaces*, 2017, **9**, 33717.
38 J. Han, W. Tian, Y. Miao, N. Li, D. Chen, Q. Xu, H. Li and J. Lu, Flexoelectricity in hydroxyapatite for the enhanced piezocatalytic degradation of phenanthrene in soil, *Ind. Chem. Mater.*, 2024, **2**, 300.
39 S. Zhang, X. Wang, S. Yin, J. Wang, H. Chen and X. Jiang, Urchin-like multiscale structured fluorinated hydroxyapatite as versatile filler for caries restoration dental resin composites, *Bioact. Mater.*, 2024, **35**, 477.
40 J. Sonamuthu, S. Samayanan, A. R. Jeyaraman, B. Murugesan, B. Krishnan and S. Mahalingam, Influences of ionic liquid and temperature on the tailorable surface morphology of F-apatite nanocomposites for enhancing biological abilities for orthopedic implantation, *Mater. Sci. Eng., C*, 2018, **84**, 99.
41 B. A. Jerri Al-Bakhsh, F. Shafiei, A. Hashemian, K. Shekofteh, B. Bolhari and M. Behroozibakhsh, In-vitro bioactivity evaluation and physical properties of an epoxy-based dental sealer reinforced with synthesized fluorine-substituted hydroxyapatite, hydroxyapatite and bioactive glass nanofillers, *Bioact. Mater.*, 2019, **4**, 322.
42 H. Huang, L. Qiang, M. Fan, Y. Liu, A. Yang, D. Chang, J. Li, T. Sun, Y. Wang, R. Guo, H. Zhuang, X. Li, T. Guo, J. Wang, H. Tan, P. Zheng and J. Weng, 3D-printed tri-element-doped hydroxyapatite/polycaprolactone composite scaffolds with antibacterial potential for osteosarcoma therapy and bone regeneration, *Bioact. Mater.*, 2024, **31**, 18.
43 V. S. Bystrov, C. Piccirillo, D. M. Tobaldi, P. M. L. Castro, J. Coutinho, S. Kopyl and R. C. Pullar, Oxygen vacancies, the optical band gap ($E_g$) and photocatalysis of hydroxyapatite: Comparing modelling with measured data, *Appl. Catal., B*, 2016, **196**, 100.
44 L. Fei, Y. Hu, X. Li, R. Song, L. Sun, H. Huang, H. Gu, H. L. W. Chan and Y. Wang, Electrospun bismuth ferrite nanofibers for potential applications in ferroelectric photovoltaic devices, *ACS Appl. Mater. Interfaces*, 2015, **7**, 3665.
45 H. You, Z. Wu, L. Zhang, Y. Ying, Y. Liu, L. Fei, X. Chen, Y. Jia, Y. Wang, F. Wang, S. Ju, J. Qiao, C. H. Lam and H. Huang, Harvesting the vibration energy of $BiFeO_3$ nanosheets for hydrogen evolution, *Angew. Chem., Int. Ed.*, 2019, **58**, 11779.